Imaging breast adipose and fibroglandular tissue molecular signatures by using hybrid MRI-guided near-infrared spectral tomography

Ben Brooksby*, Brian W. Pogue*†, Shudong Jiang*, Hamid Dehghani*, Subhadra Srinivasan*, Christine Kogel‡, Tor D. Tosteson§, John Weaver‡, Steven P. Poplack‡, and Keith D. Paulsen*

*Thayer School of Engineering, Dartmouth College, 8000 Cummings Hall, Hanover, NH 03755; and Departments of ‡Diagnostic Radiology and §Community and Family Medicine, Dartmouth Medical School, Dartmouth Hitchcock Medical Center, Lebanon, NH 03756

Edited by Britton Chance, University of Pennsylvania School of Medicine, Philadelphia, PA, and approved April 21, 2006 (received for review November 5, 2005)

Magnetic resonance (MR)-guided near-infrared spectral tomography was developed and used to image adipose and fibroglandular breast tissue of 11 normal female subjects, recruited under an institutional review board-approved protocol. Images of hemoglobin, oxygen saturation, water fraction, and subcellular scattering were reconstructed and show that fibroglandular fractions of both blood and water are higher than in adipose tissue. Variation in adipose and fibroglandular tissue composition between individuals was not significantly different across the scattered and dense breast categories. Combined MR and near-infrared tomography provides fundamental molecular information about these tissue types with resolution governed by MR T1 images.

hemoglobin | magnetic resonance imaging | water | fat | oxygen saturation

Near-infrared (NIR) imaging and spectroscopy are emerging technologies for functional characterization of biological tissues with specific information about a few important biological molecules and structures. Optical measurements of tissue have significant potential to elucidate the biochemical/structural constituents of the tissue. IR spectroscopy of tissue can be done directly or indirectly through Raman spectroscopy, and both methods have recently shown significant promise as tools to identify the biochemical components of different breast tissues (1, 2). These may become excellent intrasurgical or biopsy guides to determine which tissue should be removed, having a demonstrated sensitivity and specificity of 88% and 93%, respectively, for breast cancer microcalcifications in biopsied samples (3). These techniques measure the basic biochemical constituents such as collagen, fat, beta-carotene, cholesterol, and water and the type of calcification deposit present. The caveat of these methods is that they have short penetration and so are optimally suited for small tissue volume identification or surface imaging applications. In contrast, NIR light penetrates much further in tissue, yet has fewer and broader chemical specific absorption bands, to identify components of the tissue (4, 5) and has reported data with extremely high sensitivity and specificity for cancer based on *in vivo* studies quantifying hemoglobin and oxygenation (6). The key spectral features are from water, hemoglobin, deoxyhemoglobin, lipids, and some potential for quantifying scattering, which is due to micrometer-sized structures such as collagen and membrane-bound organelles. Thus, the microscopic constituents of tissue are identifiable with NIR imaging, yet with more macroscopic resolution than Raman spectroscopy and supplying perhaps less chemical-specific information. This work reports the previously undescribed implementation of NIR spectral imaging in a combined magnetic resonance imaging (MRI)–NIR imaging system to study identification of these biochemical features in breast adipose and fibroglandular tissues.

The potential of NIR spectroscopic measurements to determine tissue physiology and composition *in vivo* has been studied since the 1970s (7). Because NIR light can be used to propagate entirely through ≈10 cm of tissue, research has focused on applications in breast imaging (4–6, 8, 9), thereby providing this biochemical information noninvasively and in an imaging mode. In clinical breast imaging, diagnostic mammography, ultrasonography, and MRI provide structural information and comparatively little data on molecular-level changes. When contrast MRI is used, vascular function is assessed. Supplementing conventional imaging with functional information is an avenue to improve our understanding of tissues *in vivo* in both research and clinical settings. In a recent report, Chance *et al.* (6) demonstrated that NIR tomography measurements could be used for extremely high sensitivity and specificity (96% and 93%, respectively) for tumors as small as 0.8 cm. It is generally thought that the only major limitation for NIR tomography lies in the area of low spatial resolution, and if it could be implemented in a manner that used the strengths of existing clinical modalities with the benefits of NIR contrast, the modality could become an accepted tool for clinical breast cancer imaging. This work demonstrates the type of information that can be obtained with a hybrid MRI–NIR tomography system that has been optimized to produce intrinsic molecular concentrations of oxy- and deoxyhemoglobin as well as water, along with measures of the subcellular scattering response in normal breast tissue.

Relationships between NIR molecular parameters and demographic factors such as body mass index (BMI), age, hormonal status, breast size, and mammographic parenchymal pattern (i.e., radiographic density) have been investigated in the past (5, 9, 10). These studies have all been based on bulk tissue estimates, and the incorporation of conventional imaging provides an opportunity to understand how the spatial distribution of the parenchymal components within the breast affects disease incidence and progression. For example, mammography has been used in large epidemiological studies to demonstrate that radiographic density is correlated to the risk of developing cancer (11). Elucidating the causal link between density and the risk of cancer remains a challenge because the tools to evaluate breast composition are limited. In this context, NIR measurements appear to provide an independent assessment of tissue density based on scattering indices, hemoglobin, and water content (12). Hemoglobin concentration is an indicator of tissue vascularity, which is increased in breast malignancy (13, 14). Further, NIR absorption differences in tumor and normal breast tissue offer

Conflict of interest statement: No conflicts declared.

This paper was submitted directly (Track II) to the PNAS office.

Abbreviations: NIR, near-IR; SP, scattering power.

†To whom correspondence should be addressed. E-mail: pogue@dartmouth.edu.

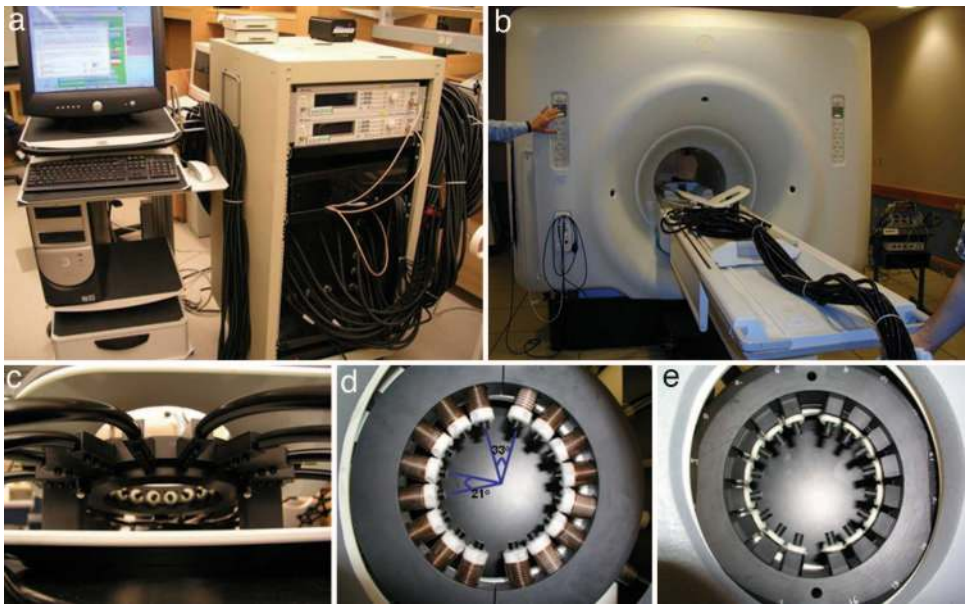

Fig. 1. The hardware systems used for integration of NIR measurements through breast tissue are shown. (*a*) Photograph of the portable NIR instrumentation and control console. (*b*) Optical fibers extend from the system into the MRI. (*c*) Open architecture breast array coil houses the optical fiber positioning system and allows for ≈8 cm of vertical motion. (*d* and e) The first (*d*) and second (e) generation MR-compatible fiber-positioning mechanisms.

one of the highest intrinsic biological contrasts available in medical imaging, being up to 200% or more, which is equivalent to the contrast available in x-ray imaging of microcalcifications. Lower levels of oxygen saturation also have been found in malignancies, a consequence of tumor cell proliferation combined with compromised perfusion and supply rate mechanisms (15). MRI-guided NIR spectral tomography offers the possibility of monitoring these physiological and pathophysiological changes with high resolution.

Multimodality imaging is increasingly being used to interrogate tissue morphology and function simultaneously because of the inherent benefit of optimized coregistration. Initial demonstrations of MRI-guided NIR tomography was demonstrated by Ntziachristos *et al.* (16) in breast tumor imaging. The present work explores the integration of MRI (structural) and NIR tomography (functional) into a single platform for the study of breast tissue. Significant improvement in the stability and accuracy of the reconstruction process can be obtained through MRI segmented anatomical information as an input to the NIR parameter estimation problem. However, the way in which the prior information is used is critical (17–22). Misguided constraints can lead to errors that are detrimental to the image outcome. To date, NIR techniques have been combined with several high-spatial-resolution, structure-bearing imaging modalities, including x-ray tomosynthesis (23), ultrasound (24), and MRI (25, 26), to study human tissues and small animals. Here, integration of tissue structure is achieved by partitioning the regularization matrix according to the MRI segmentation and by using a Laplacian mathematical construct (22, 26). The approach seamlessly integrates MRI priors into a multispectral NIR tomography reconstruction and allows molecular imaging of the different tissue compositions within the breast. The work shows previously undescribed cross-sectional NIR images of molecular signatures known to exist in breast tissue where the spatial boundaries are preserved by MRI. A pilot population of healthy female volunteers has been imaged and the properties of adipose and fibroglandular tissues are examined to identify variations in composition within the breast and between subjects.

Results

Image and Data Acquisition. The tomographic imaging system, described in detail by Brooksby *et al.* (27) and shown in Fig. 1, records measurements of NIR light transmission through a pendant breast in a planar, anatomically coronal geometry. The NIR and T1-MRI data acquisition occur in parallel with a total examination time of <10 min. Full-volume T1-weighted MR scans are acquired (50 coronal slices, 25-ms repetition time (TR), 6-ms time to echo (TE), 45° flip angle, 2-mm slice thickness), which provide a map of tissue structure with millimeter spatial resolution that clearly differentiates adipose from fibroglandular tissue. Anatomically axial and coronal slices from three representative cases are shown in columns 1 and 2 of Fig. 2, respectively. The coronal MR slices show the structure of the breast in the plane of optical measurement, and the bright spots around the tissue perimeter represent fiducial markers attached to each optode. The age and radiographic density of these women were 65, 52, and 43, and scattered, extremely dense, and heterogeneously dense, respectively. There are few similarities in the parenchymal patterns in these three breasts. Grayscale values in the first (Fig. 2 *Top*) indicate predominantly adipose composition intermixed with small amounts of vasculature and fibroglandular tissue. The second case (Fig. 2 *Middle*) appears to contain predominantly fibroglandular tissue intermixed with fat, whereas the third (Fig. 2 *Bottom*) shows a well differentiated layer of surrounding adipose tissue.

The MRI-guided NIR reconstruction technique was applied, and reconstructed images of total hemoglobin concentration ($[Hb_T]$, μM) are presented in column 4 of Fig. 2. High contrast is observed with MR-like resolution. In each case, fibroglandular tissue shows higher $[Hb_T]$ than adipose tissue. This result is expected because more vessels are found in fibroglandular breast than in the fibrous and adipose stroma. Three additional cases are shown in Fig. 3. Here, reconstructed images of additional NIR parameters have been included: $[Hb_T]$, hemoglobin oxygen saturation (S_tO_2, %), water fraction (H_2O, %), scattering amplitude (A), and scattering power (SP). Interestingly, the spatial distributions in the NIR images do not exactly match the segmented MRI regions in all cases, and some heterogeneity

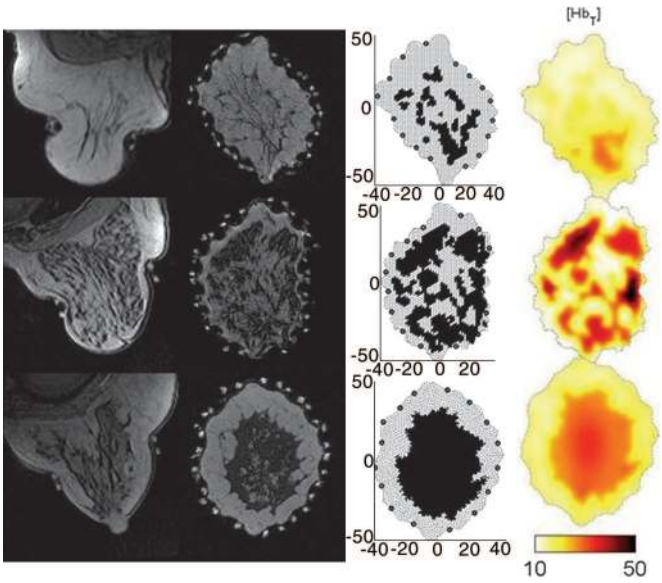

Fig. 2. Breast images are displayed from MRI and NIR. Anatomically axial (column 1 from left) and coronal (column 2) T1-weighted MR scans through three normal breasts. The coronal slices correspond to the plane of NIR measurement. Fiducial markers attached to each optical fiber are visible at the tissue perimeter and are projected onto the model surface (as dots in column 3). Coronal slices are used to create 2D meshes (column 3), which accurately represent the breast structure in the plane of interest, as well as to locate the measurement positions with millimeter accuracy. Each mesh location (node) is classified to define either adipose or fibroglandular tissue based on segmentation of the MRI grayscale intensities, and the dimensions are shown in millimeters, in the middle column of breast meshes. These meshes are used in the NIR image reconstruction from simultaneously acquired optical data. Images of the corresponding total hemoglobin concentration ([Hb_T], μM) are shown in column 4.

occurs, although the predominant effect is the significant change in optical properties that results between the adipose and fibroglandular boundaries.

Table 1. Average values, SDs, and total ranges for total hemoglobin concentration, hemoglobin oxygen saturation, water fraction, scattering amplitude, and scattering power of adipose and fibroglandular tissue

	Adipose tissue		Glandular tissue	
Property	Mean ± SD	Total range	Mean ± SD	Total range
Hb_T concentration, μM	17.1 ± 3.2	11.7–22.9	22.4 ± 7.3	9.8–35.6
S_tO_2, %	70.7 ± 8.6	51.8–77.4	69.7 ± 10.4	38.8–80.2
Water fraction, %	46.8 ± 18.5	23.0–78.5	60.3 ± 23.6	17.5–93.5
A	1.34 ± 0.54	0.86–2.77	0.94 ± 0.38	0.32–1.79
SP	0.56 ± 0.32	0.00–0.94	0.79 ± 0.48	0.00–1.36

Summary of Breast Data. Cumulative results are presented in Table 1 for the 11 subjects enrolled in the study. All parameters lie within, or overlap the ranges of, the bulk average breast properties measured previously (4, 5, 8–10), which uniformly report large intersubject variations in the NIR estimations. Based on the standard deviations observed here, SP shows the highest relative variability between subjects (61% in fibroglandular tissue), and hemoglobin oxygen saturation shows the lowest (12% in adipose tissue). Chromophore concentration intersubject variations were not significantly different between fibroglandular and adipose tissue (Table 1). Numerical values in Table 1 are plotted graphically in Fig. 4.

The differences in the optical properties of the two predominant tissue types were analyzed. Table 2 shows that S_tO_2 is the only parameter not significantly different in adipose versus fibroglandular tissue in all 11 exams. These trends match several expectations based on physiology. Specifically, fibroglandular tissue is known to contain more blood vessels than adipose and to have a greater blood supply and water content (28). The connection between physiology and NIR scattering parameters *A* and SP is less clear. However, one *ex vivo* validation of these findings is provided by Peters *et al.* (29), who measured the scattering spectrum of excised breast tissue in the NIR wave-

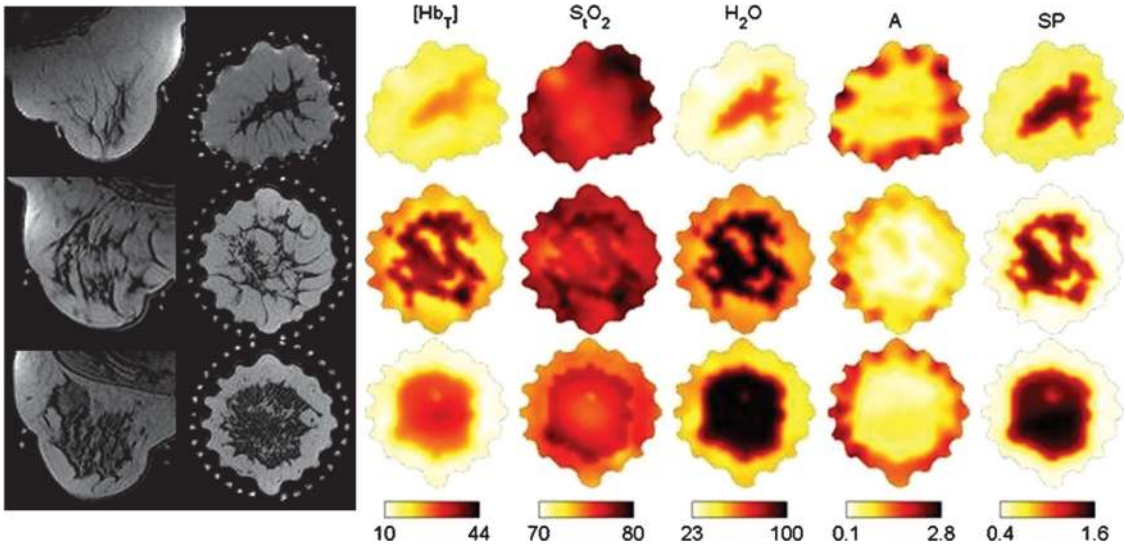

Fig. 3. Breast images are displayed for MRI and NIR. Anatomically axial (column 1 from left) and coronal (column 2) T1-weighted MRI slices through three normal breasts. Subjects were 69, 43, and 43 years old with scattered (*Top*), heterogeneously dense (*Middle*), and heterogeneously dense (*Bottom*) radiodensities, respectively. (Columns 3–7) Reconstructed images of chromophores and scatter parameters from simultaneously acquired NIR measurements (left to right) are as follows: total hemoglobin concentration ([Hb_T], μM), hemoglobin oxygen saturation (S_tO_2, %), water fraction (H_2O, %), scattering amplitude (*A*), and *SP*. The spatial dimensions are similar to Fig. 2, with all breasts being ≈8–10 cm in diameter.

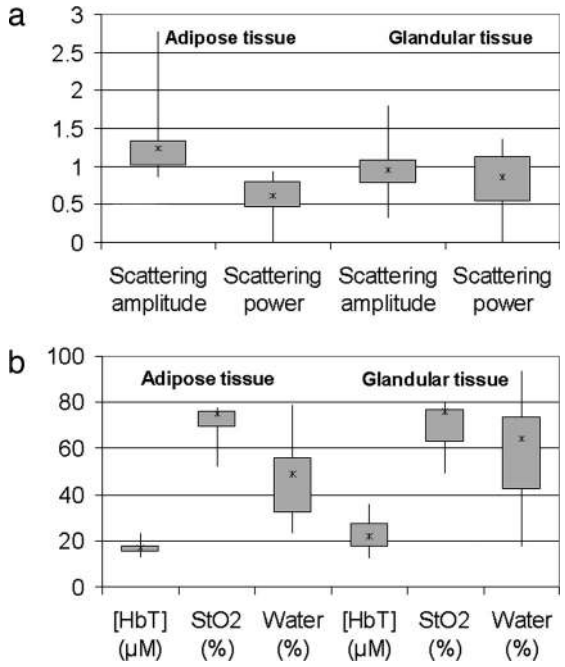

Fig. 4. Box plots of average properties for adipose and fibroglandular tissues, including scattering parameters of amplitude and power (*a*), and hemoglobin concentration [Hb_T], oxygen saturation (S_tO_2), and water fraction (*b*). Bars represent the total range in the values within each tissue type.

length range and observed a higher SP in fibroglandular components. It is likely that scattering amplitude and power are surrogate measures of particle density and size, respectively (30, 31), but experimental confirmation is an area of active research.

Discussion

The segmented MRI in the NIR imaging plane provides estimates of the percentage of adipose tissue by area, which was used to guide data analysis and ranged from 49% to 86%, with an average of 70% in the 11 subjects evaluated. We observed a correlation between age and percent adipose tissue ($r = 0.69$, $P = 0.02$), and a paired t test confirmed that women with scattered radiographic density had a higher adipose content than those with heterogeneously dense, or extremely dense, breast classifications ($r = 0.30$, $P = 0.001$). In previous work, adipose fraction was seen as a correlate to body mass index, which likely represents the fact that higher body mass correlates with increase fat content in most women (9). Results from stand-alone NIR imaging systems, which probe the entire breast, have produced correlations with age, radiographic density, and body mass index (9, 10, 32) that could reflect changes in the volume fraction of adipose and fibroglandular tissues, rather than changes in their individual compositions. Pifferi *et al.* (32) noted significant variation in the scattering parameters existed both between breasts and even spatially within the breast tissue of an individual. It is likely that MRI-guided NIR tomography will elucidate the origin of this heterogeneity, because the spatial variation in the adipose and fibroglandular tissues can be dissected from the MRI images. Correlation coefficients and associated P values were calculated for relationships between age, percent adipose tissue, and the NIR parameters. No correlation was observed between subject age and any of these tissue characteristics, supporting the assumption that the intrinsic characteristics of fat, for example, do not change with age regardless of findings from previous studies. Percent adipose tissue did correlate with adipose oxygen saturation ($r = 0.66$, $P = 0.027$), although it is not immediately obvious why these two parameters should be related. In addition to age, the relative abundance of adipose and fibroglandular tissue is known to depend on the subject's weight, race, and behavioral factors.

Relationships between NIR parameters derived from the two tissue types also were studied. The only significant connection appears between water and oxygen saturation for fibroglandular tissue ($r = 0.70$, $P = 0.015$). We assessed the relationship between radiographic density and NIR properties for adipose and fibroglandular tissue as well. Table 2 showed that none of the NIR parameters for fat were significantly different between breasts with different radiodensity classifications. Similarly, most of the fibroglandular tissue parameters did not differ, except hemoglobin, which did correlate with increasing density for this tissue type. It is currently unknown whether the composition of fibroglandular tissue is truly different in breasts scored in these different density categories. It could be that the vascular compartment within the fibroglandular zone is greater in the denser breast. Another explanation for the difference observed here may be found in Fig. 2. It is clear that the parenchyma patterns for women with different densities can vary, and it is well known that during menopause, with the cessation of ovarian hormonal function, breast lobules in glandular tissue atrophy; hence, the relative adipose and fibrous stromal volumes may increase. It is also possible that the resolution of the MRI–NIR image segmentation is too coarse to capture accurately parenchymal distributions for image reconstruction, especially in scattered densities. The size of associated fibroglandular regions may be overestimated, leading to an underestimation of the localized absorption contrast due to hemoglobin by means of an averaging effect with the adjacent misclassified fat that actually exists.

The study presented here demonstrates the capability of MR-guided NIR imaging. The technique provides high-resolution images of both tissue structure through MRI and tissue function through NIR contrast. The incorporation of anatomical information indicates that improved NIR image quality is achieved and will likely increase the potential for relevant physiological investigation. It appears increasingly probable that optical techniques will play important clinical roles when combined with other imaging systems, as recently demonstrated by Chance *et al.* (6), demonstrating high sensitivity and specificity values when imaging breast cancer tumors. For example, optical signatures can be specific to molecular changes in tissue, as recently demonstrated with Raman spectroscopy (1, 3), and use of vascular permeability agents (33), lymphatic agents (34), and/or molecular specific contrast agents (35) in this sort of tomography geometry will likely lead to useful diagnostic testing for specific disease processes. Integrating optical imaging with MRI may provide enhanced information about hemodynamics and metabolism at minimal additional cost and complexity compared with the

Table 2. *P* values from paired *t* tests on differences between NIR-derived properties associated with tissue type with adipose vs. glandular tissue in scattered vs. dense breasts

	Adipose vs. glandular	Scattered ($n = 6$) vs. dense ($n = 5$)	
Property	Mean diff.	Adipose, mean diff.	Glandular mean diff.
$[Hb_T]$	0.022*	0.902	0.009*
S_tO_2	0.798	0.166	0.170
Water	0.040*	0.769	0.068
A	0.005*	0.673	0.579
SP	0.045*	0.324	0.892

All numbers are P values. Adipose vs. glandular, $n = 11$; scattered, $n = 6$; dense, $n = 5$. *, $P < 0.05$.

MR system itself. In using this type of a hybrid system, care has been taken to apply it to two well understood tissue types first, namely adipose and fibroglandular tissues, which have very well known differences in vascular volume, fat, and water composition. Use of the system in more complex and less well understood tissues, such as different types of tumors, will require extensive validation with independent methods. It is not clear at this time whether this system will be successful in characterizing or detecting small tumors; based on phantom studies it does appear that it will be more accurate that a stand-alone NIR tomography system.

Although this study presents an important step in the development of a hybrid system for MRI and optical tomography, further questions clearly remain as to the functionality and utility of the system. A priority is validation of the chromophore quantification, and only extensive phantom studies with complex phantom geometries mimicking the interior complexity of the breast will suffice for this validation. Initial studies with three-layer phantoms, in previous papers, indicate that hemoglobin quantification in broad regions is possible (22, 26, 36, 37). More complex and highly heterogeneous phantoms should be analyzed in the future to ensure the accuracy of this type of hybrid system and to determine what the minimum resolution and "effective" complexity is possible to segment out from the background tissue for this type of volumetric NIR spectroscopy. In addition, further validation of the quantification of water is possible by comparison with water quantification in MRI (38). Initial data in this area are encouraging, yet concerns about the ability to quantify water concentration with MRI remain and will always have some level of uncertainty, because of the varying MR spectrum of bound vs. unbound water.

Materials and Methods

Human Subjects. An MR-guided NIR imaging system was used to study the breast tissue properties of 11 women with normal mammography. The Institutional Review Board at the Dartmouth Hitchcock Medical Center approved the clinical examination protocol, and written informed consent was obtained from all subjects before participation. The average age of the volunteers was 53 years and ranged from 43 to 69 years. Four of the women were premenopausal, and seven were postmenopausal, none of whom were taking hormone replacement therapy. Six of the women had scattered radiographic density, four were heterogeneously dense, and one was extremely dense. Given the accurate MR coregistration, each NIR property image location was associated with either adipose or fibroglandular tissue, and the average properties of each tissue, along with their standard deviation and total range across the subject pool, were determined.

Imaging System Design. The NIR imaging system consisted of six laser diodes (660–850 nm), which were amplitude-modulated at 100 MHz. The bank of laser tubes was mounted on a linear translation stage that sequentially coupled the activated source into 16 bifurcated optical fiber bundles. The central seven fibers delivered the source light, while the remaining fibers collected transmitted light and were coupled to photomultiplier tube (PMT) detectors. For each source, measurements of the amplitude and phase shift of the 100-MHz signal were acquired from 15 locations around the breast. As shown in Fig. 1*b*, the fibers extended 13 m into a 1.5-T whole-body MRI (GE Medical Systems), and the two data streams (i.e., NIR and MRI) were acquired simultaneously. The participant lay on an open architecture breast array coil (Invivo, Orlando, FL), shown in Fig. 1*c*, which also houses the MR-compatible fiber positioning system. The plane of fibers spanning the circumference of a pendant breast can be positioned manually from nipple to chest wall if multiple planes of NIR data are desired. Two fiber-breast interface prototypes were constructed. The first, pictured in Fig. 1*d*, allows each of the 16 fibers to move independently in a radial direction, and tissue contact is enforced with bronze compression springs. The second, shown in Fig. 1*e*, maintains a circular breast circumference and allows more user control. Generally, we have observed that NIR data quality and image reconstruction is more effective on circular geometries than on some of the distended shapes commonly observed with the first design. This finding was anticipated by Pogue *et al.* (39), who showed that geometries that maximize symmetry in the projection angles between source and detectors often yield the best images.

Image Reconstruction Algorithm. Image reconstruction has been outlined in detail in previous papers (22, 26), but the salient features are summarized here. A frequency-domain diffusion model was used to simulate measured signals for any specified distribution of absorption and reduced scattering coefficients, μ_a and μ_s', within an imaged volume given by

$$-\nabla\cdot D(r)\nabla\phi(r,\ \omega) + \left(\mu_a(r) + \frac{i\omega}{c}\right)\phi(r,\ \omega) = S(r,\ \omega), \qquad [1]$$

where $S(r, \omega)$ is an isotropic light source and $\phi(r, \omega)$ is the photon density at position r; c is the speed of light in tissue; ω is the frequency of light modulation; and $D = 1/[3(\mu_a + \mu_s')]$ is the diffusion coefficient. Customized software tools were used to automatically create meshes in which each location corresponded to either adipose or fibroglandular tissue as illustrated in Fig. 2.

Having obtained the measurements at the periphery of the breast, image reconstruction was carried out by repeated solution of Eq. **1** to estimate the chromophore concentrations and scattering parameters. The inversion process minimized the least-squares functional

$$\chi^2 = \sum_{j=1}^{Mn} (\phi_j^m - \phi_j^c)^2 + \beta \sum_{j=1}^{Mn} L(\mu_j - \mu_{o,j})^2, \qquad [2]$$

where Mn is the total number of measurements at all wavelengths (240×6), and ϕ_j^m and ϕ_j^c are, respectively, the measured and calculated fluence at the boundary for each measurement point j. β is the regularizing factor for the spatial prior, and L is a matrix generated from MRI-derived spatial data, acting on the solution μ. L links all of the locations in a particular type tissue (fibroglandular or fatty) and respects the MR-defined internal boundaries by applying a second differential, Laplacian-shaped operator to each region separately (26). The effect is similar to that of total variation minimization (40) because it allows sharp boundary transitions to exist but provides the flexibility to encode these boundaries from MRI information and has the effect of smoothing continuous regions. Spectral relationships for absorption from Beer's law and scattering based on Mie theory were incorporated into the reconstruction directly (41). Beer's law states that $\mu_a(\lambda) = \sum_{i=0}^{n} [\varepsilon(\lambda)]c_i$, where $\varepsilon(\lambda)$ is the molar absorption spectra of the absorbing tissue chromophores each having concentration c_i. Similarly, a power law $\mu_s'(\lambda) = A\lambda^{-SP}$ describes the relationship between the reduced scattering coefficient, A, and SP (42). The minimization of Eq. **2** is accomplished with a Newton–Raphson iterative method by using a modified Levenberg–Marquardt approach to regularization, and the final matrix equation that is solved is (21)

$$(\tilde{J}^T\tilde{J} + \beta L^T L)\partial\mu = \tilde{J}^T\partial\phi. \qquad [3]$$

β is set to 10 times the maximum value of the diagonal of $\tilde{J}^T\tilde{J}$. This value was determined in previous studies (26) and appears optimal regardless of the complexity of the regional distribution of the imaged volume encoded in L.

Statistical Analysis of Data. Statistical analysis of the data was completed with a standard paired t test on differences between the NIR-derived properties associated with the two tissue types adipose and fibroglandular, to examine whether there was a difference in composition between scattered and dense breasts.

This work was supported by National Institutes of Health Grants R01CA69544 and P01CA80139.

1. Shafer-Peltier, K. E., Haka, A. S., Fitzmaurice, M., Crowe, J., Myles, J., Dasari, R. R. & Feld, M. S. (2002) *J. Raman Spectrosc.* **33,** 552–563.
2. Xu, Y. Z., Zhao, Y., Xu, Z., Ren, Y., Liu, Y. H., Zhang, Y. F., Zhou, X. S., Shi, J. S., Xu, D. F. & Wu, J. G. (2005) *Spectrosc. Spectral Anal.* **25,** 1775–1778.
3. Haka, A. S., Shafer-Peltier, K. E., Fitzmaurice, M., Crowe, J., Dasari, R. R. & Feld, M. S. (2002) *Cancer Res.* **62,** 5375–5380.
4. Cerussi, A. E., Berger, A. J., Bevilacqua, F., Shah, N., Jakubowski, D., Butler, J., Holcombe, R. F. & Tromberg, B. J. (2001) *Academic Radiol.* **8,** 211–218.
5. Pogue, B. W., Jiang, S., Dehghani, H., Kogel, C., Soho, S., Srinivasan, S., Song, X., Tosteson, T. D., Poplack, S. P. & Paulsen, K. D. (2004) *J. Biomed. Opt.* **9,** 541–552.
6. Chance, B., Nioka, S., Zhang, J., Conant, E. F., Hwang, E., Briest, S., Orel, S. G., Schnall, M. D. & Czerniecki, B. J. (2005) *Academic Radiol.* **12,** 925–933.
7. Jobsis, F. F. (1977) *Science* **198,** 1264–1267.
8. Durduran, T., Choe, R., Culver, J. P., Zubkov, L., Holboke, M. J., Giammarco, J., Chance, B. & Yodh, A. G. (2002) *Phys. Med. Biol.* **47,** 2847–2861.
9. Srinivasan, S., Pogue, B. W., Jiang, S., Dehghani, H., Kogel, C., Soho, S., Chambers, J. G., Tosteson, T. D., Poplack, S. P. & Paulsen, K. D. (2003) *Proc. Natl. Acad. Sci. USA* **100,** 12349–12354.
10. Shah, N., Cerussi, A., Eker, C., Espinoza, J., Butler, J., Fishkin, J., Hornung, R. & Tromberg, B. J. (2001) *Proc. Natl. Acad. Sci. USA* **98,** 4420–4425.
11. Boyd, N. F., Lockwood, G. A., Byng, J. W., Tritchler, D. L. & Yaffe, M. J. (1998) *Cancer Epidemiol. Biomarkers Prev.* **7,** 1133–1144.
12. Simick, M. K., Jong, R., Wilson, B. C. & Lilge, L. (2004) *J. Biomed. Opt.* **9,** 794–803.
13. Hasan, J., Byers, R. & Jayson, G. C. (2002) *Br. J. Cancer* **86,** 1566–1577.
14. Marson, L. P., Kurian, K. M., Miller, W. R. & Dixon, J. M. (2001) *Breast Cancer Res. Treat.* **66,** 9–15.
15. Vaupel, P. & Harrison, L. (2004) *Oncologist* **9,** Suppl. 5, 4–9.
16. Ntziachristos, V., Yodh, A. G., Schnall, M. & Chance, B. (2000) *Proc. Natl. Acad. Sci. USA* **97,** 2767–2772.
17. Barbour, R. L., Graber, H. L., Chang, J., Barbour, S. S., Koo, P. C. & Aronson, R. (1995) *IEEE Comp. Sci. Eng.* **2,** 63–77.
18. Pogue, B. W. & Paulsen, K. D. (1998) *Opt. Lett.* **23,** 1716–1718.
19. Kaipio, J. P., Kolehmainen, V., Vauhkonen, M. & Somersalo, E. (1999) *Inverse Problems* **15,** 713–729.
20. Schweiger, M. & Arridge, S. R. (1999) *Phys. Med. Biol.* **44,** 2703–2721.
21. Borsic, A., Lionheart, W. R. B. & McLeod, C. N. (2002) *IEEE Trans. Med. Imaging* **21,** 579–588.
22. Brooksby, B., Srinivasan, S., Jiang, S., Dehghani, H., Pogue, B. W., Paulsen, K. D., Weaver, J., Kogel, C. & Poplack, S. P. (2005) *Opt. Lett.* **30,** 1968–1970.
23. Li, A., Miller, E. L., Kilmer, M. E., Brukilaccio, T. J., Chaves, T., Stott, J., Zhang, Q., Wu, T., Choriton, M., Moore, R. H., *et al.* (2003) *Appl. Opt.* **42,** 5181–5190.
24. Zhu, Q., Chen, N. G. & Kurtzman, S. H. (2003) *Opt. Lett.* **28,** 337–339.
25. Ntziachristos, V., Yodh, A. G., Schnall, M. D. & Chance, B. (2002) *Neoplasia* **4,** 347–354.
26. Brooksby, B., Jiang, S., Dehghani, H., Pogue, B. W., Paulsen, K. D., Weaver, J., Kogel, C. & Poplack, S. P. (2005) *J. Biomed. Opt.* **10,** 051504.
27. Brooksby, B. A., Jiang, S., Dehghani, H., Kogel, C., Doyley, M., Weaver, J. B., Poplack, S. P., Pogue, B. W. & Paulsen, K. D. (2004) *Rev. Sci. Instrum.* **75,** 5262–5270.
28. Thomsen, S. & Tatman, D. (1998) *Ann. N.Y. Acad. Sci.* **838,** 171–193.
29. Peters, V. G., Wyman, D. R., Patterson, M. S. & Frank, G. L. (1990) *Phys. Med. Biol.* **35,** 1317–1334.
30. Wang, X., Pogue, B. W., Jiang, S., Song, X., Paulsen, K. D., Kogel, C., Poplack, S. P. & Wells, W. A. (2005) *J. Biomed. Opt.* **10,** 051704.
31. Wang, X., Pogue, B. W., Jiang, S., Dehghani, H., Song, X., Srinivasan, S., Brooksby, B. A., Paulsen, K. D., Kogel, C., Poplack, A. P. & Wells, W. A. (2006) *J. Biomed. Opt.*, in press.
32. Pifferi, A., Swartling, J., Chikoidze, E., Torricelli, A., Taroni, P., Bassi, A., Andersson-Engels, S. & Cubeddu, R. (2004) *J. Biomed. Opt.* **9,** 1143–1151.
33. Pogue, B. W. (2006) *Academic Radiol.* **13,** in press.
34. Kim, S., Lim, Y. T., Soltesz, E. G., De Grand, A. M., Lee, J., Nakayama, A., Parker, J. A., Mihaljevic, T., Laurence, R. G., Dor, D. M., *et al.* (2003) *Nat. Biotechnol.* **22,** 93–97.
35. Lenkinski, R. E., Ahmed, M., Zaheer, A., Frangioni, J. V. & Goldberg, S. N. (2003) *Acad. Radiol.* **10,** 1159–1164.
36. Brooksby, B. A., Dehghani, H., Pogue, B. W. & Paulsen, K. D. (2003) *IEEE J. Selected Top. Quant. Electronics* **9,** 199–209.
37. Brooksby, B. (2005) Ph.D. thesis (Dartmouth College, Hanover, NH).
38. Brooksby, B., Jiang, S., Dehghani, H., Pogue, B. W., Paulsen, K. D., Weaver, J. B., Kogel, C. & Poplack, S. P. (2006) *Proc. SPIE Int. Soc. Opt. Eng.*, in press.
39. Pogue, B. W., McBride, T. O., Osterberg, U. L. & Paulsen, K. D. (1999) *Opt. Express* **4,** 270–287.
40. Paulsen, K. D., Jiang, H. (1996) *Appl. Opt.* **35,** 3447–3458.
41. Srinivasan, S., Pogue, B. W., Brooksby, B., Jiang, S., Dehghani, H., Kogel, C., Wells, W. A., Poplack, S. & Paulsen, K. D. (2005) *Technol. Cancer Res. Treat.* **4,** 513–526.
42. van Staveren, H. J., Moes, C. J. M., van Marle, J., Prahl, S. A. & van Gemert, M. J. C. (1991) *Appl. Opt.* **30,** 4507–4514.